CM² MAGAZINE

第 47 期

南方科技大学海洋磁学中心主编

创刊词

海洋是生命的摇篮，是文明的纽带。地球上最早的生命诞生于海洋，海洋里的生命最终进化成了人类，人类的文化融合又通过海洋得以实现。人因海而兴。

人类对海洋的探索从未停止。从远古时代美丽的神话传说，到麦哲伦的全球航行，再到现代对大洋的科学钻探计划，海洋逐渐从人类敬畏崇拜幻想的精神寄托演变成可以开发利用与科学研究的客观存在。其中，上个世纪与太空探索同步发展的大洋科学钻探计划将人类对海洋的认知推向了崭新的纬度：深海（deep sea）与深时（deep time）。大洋钻探计划让人类知道，奔流不息的大海之下，埋藏的却是亿万年的地球历史。它们记录了地球板块的运动，从而使板块构造学说得到证实；它们记录了地球环境的演变，从而让古海洋学方兴未艾。

在探索海洋的悠久历史中，从大航海时代的导航，到大洋钻探计划中不可或缺的磁性地层学，磁学发挥了不可替代的作用。这不是偶然，因为从微观到宏观，磁性是最基本的物理属性之一，可以说，万物皆有磁性。基于课题组的学科背景和对海洋的理解，我们对海洋的探索以磁学为主要手段，海洋磁学中心因此而生。

海洋磁学中心，简称 CM^2，一为其全名“Centre for Marine Magnetism”的缩写，另者恰与爱因斯坦著名的质能方程 $E = MC^2$ 对称，借以表达我们对科学巨匠的敬仰和对科学的不懈追求。

然而科学从来不是单打独斗的产物。我们以磁学为研究海洋的主攻利器，但绝不仅限于磁学。凡与磁学相关的领域均是我们关注的重点。为了跟踪反映国内外地球科学特别是与磁学有关的地球科学领域的最新研究进展，海洋磁学中心特地主办 CM^2 Magazine，以期与各位地球科学工作者相互交流学习、合作共进！

“海洋孕育了生命，联通了世界，促进了发展”。 21 世纪是海洋科学的时代，由陆向海，让我们携手迈进中国海洋科学的黄金时代

目 录

研究进展

孟俊：白垩纪广阔的大印度岩石圈

地球是目前探测到唯一具有板块构造的行星。美国国家研究理事会发布的《时域地球——美国国家科学基金会地球科学十年愿景（2020-2030）》将“板块起源”列入优先科学问题。解决板块起源问题的关键在于如何更全面地定义板块构造现今是什么以及曾经是什么。白垩纪以来，从冈瓦纳超大陆裂解出的印度板块北缘俯冲至欧亚大陆之下，创造了“世界屋脊”青藏高原。科学家将这部分消失的岩石圈称为“大印度板块”。 定义大印度板块的大小是定量确定大陆岩石圈俯冲规模和约束印度-欧亚碰撞位置的前提，是理解青藏高原双倍地壳形成机制的钥匙。那么，大印度板块究竟有多大？

特提斯喜马拉雅地块代表了印度被动大陆边缘，其白垩纪古纬度是解决大印度重建的关键科学问题。我校地球科学与资源学院王成善院士团队孟俊副教授与德国慕尼黑大学 Stuart Gilder 教授合作，对印度大陆北缘特提斯喜马拉雅地块东部错那地区、中部仲巴地区和西部札达地区白垩系开展了构造古地磁学研究，获得特提斯喜马拉雅地块东部和中西部早白垩世（130 Ma）古地磁极分别为 22.0°N, 266.7°E, A_{95}=7.6° 和 29.7°N, 260.1°E, A_{95}=4.9°，古纬度分别为 39.6±7.6°S 和 30.5±4.9°S；特提斯喜马拉雅地块西部晚白垩世（70 Ma）古地磁极为−33.4 °N, 5.7 °E (d_p = 1.6°, d_m = 3.2°, S = 11.1, K = 53.7)，古纬度为 5.0 ± 1.6 °N；并通过经线大圆弧与古纬度交汇的新方法定量恢复了白垩纪以来俯冲消减的大印度岩石圈大小，取得的创新性成果主要有：

（1）印度-欧亚大陆碰撞之前，大印度岩石圈的中西部和东部宽度远远大于现今的喜马拉雅造山带，分别为～2700 km 和 ～2000 km；

（2）印度-欧亚碰撞带西部碰撞启动时间为 55 ± 5Ma；

（3）面积至少为 4.7 × 10^6 km^2 的大印度岩石圈俯冲至欧亚大陆之下，俯冲后的大印度地壳所产生的浮力可以造成青藏高原的隆升。

（4）大印度北缘形态决定了现今的印度-欧亚板块边界形态。

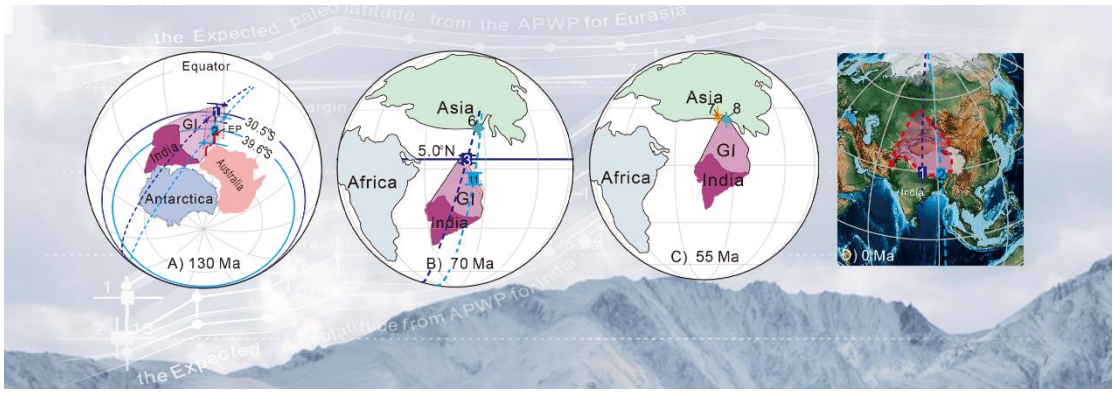

上述研究成果分别发表在地球科学国际权威刊物《Earth and Planetary Science Letters》和《Geophysical Research Letters》（封面文章）上。慕尼黑大学官方对中德科研合作成果进行了研究亮点报道（https://www.en.uni-muenchen.de/news/newsarchiv/2019/gilder_indianplate.html）。

（1） Meng, J., Gilder S.A., Li Y.L., Wang C.S., and Liu T., 2020, Expanse of Greater India in the late Cretaceous, Earth and Planetary Science Letters, 542, 116330, doi:10.1016/j.epsl.2020.116330.

（2） Meng, J., Gilder, S. A., Wang, C., Coe, R. S., Tan, X., Zhao, X., and He, K, 2019, Defining the Limits of Greater India. Geophysical Research Letters (封面文章), 46. https://doi.org/10.1029/2019GL082119。

全文链接：

https://www.sciencedirect.com/science/article/abs/pii/S0012821X20302740；

https://agupubs.onlinelibrary.wiley.com/doi/abs/10.1029/2019GL082119

岩石磁学演绎

第 37 章　磁性分离技术

自然样品通常包含多种磁性矿物，每种组分的来源和粒径各有不同，有必要用物理、化学或者数学方法分离出各个组分的信息。对于磁化率来说，因为不同组分反应的环境过程各不相同，不宜一概而论，所以这种信息分离显得非常必要。

一种分离信息的方法是通过组合使用简单的参数（如 ARM、不同外场下获得的 IRM 以及这些参数的比值，比如 HIRM，S-ratio 和 L-ratio），对于鉴别样品中主要的磁性矿物是有效的[*e.g., Roberts et al.*, 1995; *Maher and Thompson*, 1999, p. 42]. 不过，该方法局限性很大，因为天然样品的磁性矿物通常比较复杂，具有多种磁畴状态，阳离子替代现象普遍等特征，这些因素都能造成数据解释的困难。*Lowrie* [1990]提出一个简单易行的方法分离混合矿物的矫顽力信息，即三轴实验。该方法沿三个正交方向，依次施加强中弱三个外场，样品获得三个正交的 IRM。第一个方向上的 IRM 由强矫顽力的颗粒携带，最后一个方向上的 IRM 由矫顽力较小的组分携带。接下来，对样品进行分步热退磁。这样，三轴的退磁数据分别反映了矫顽力强中弱三个组分的解阻温度谱，提供了相对丰富的信息。*Roberts et al.* [1995] 和 *Maher and Thompson* [1999]设计了流程图，通过有序地测量获得矫顽力，热稳定性和粒径分布的信息从而鉴别矿物。*France and Oldfield* [2000] 的书中也提到了相似的方法，他们的流程依次为高场（>2 T），正交退磁以及在-196-680 ºC 之间对 SIRM 进行冷却加热。高矫顽力的特征是鉴别赤铁矿和针铁矿的重要依据 [*France and Oldfield*, 2000; *Maher et al.*, 2004]。

磁选是常用的物理分离方法，可以将强磁性矿物从弱磁性的基质中提取出来 [*e.g., Petersen et al.*, 1986; *Stoltz et al.*, 1986; *Hesse*, 1994; *Hounslow and Maher*, 1996]。不过对于像赤铁矿和针铁矿这样的弱磁性矿物来说，分离的效果不理想 [*Liu et al.*, 2003]。利用重力沉降可以将样品分离成不同粒径的组分。尤其是利用重液分离得到的磁性矿物，具有和原始样品相似的矫顽力分布 [*Franke et al.*, 2007]。

另一种方法是按照粒径大小分选矿物。不同于磁选，该方法不会遗漏磁性组分从而能更可信地分析物源沉积物。步骤为先用六偏磷酸钠将沉积物分解，然后进行筛选和吸取，这样就可以得到适合磁学测量的组分。针对灰尘和气溶胶样品使用该方法，有助于更真实地对比沉降物质与源区物质[Lyons et al., 2012]；而对古土壤，该方法有助于分离整体测量信息从而让研究者能够分别评价碎屑和成土作用组分的信息[Hao et al., 2008]。对于湖相沉积物，筛除生物成因组分后的样品才适合用来研究沉积物源的信息[Hatfield and Maher, 2009]。

CBD 方法（柠檬酸-碳酸氢钠-亚硫酸钠）是常用的化学分离方法。这种方法能非常有效地溶解土壤和古土壤中的小粒径的 Fe^{3+}矿物，比如赤铁矿，针铁矿和磁赤铁矿[*Mehra and Jackson*, 1958; *Verosub et al.*, 1993]，也可能适用于小粒径的磁铁矿[*Hunt et al.*, 1995c]。当土壤的整体磁学性质主要受成岩作用组分的影响时，用 CBD 提取的 Fe 可以很好的反映成土作用[*Liu et al.*, 2010]。土壤中结晶不好的氧化物（如水铁矿）可以利用酸性草酸铵去除[*Cornell and Schwertmann*, 2003]。

由于不同矿物热稳定性的差异，低温和高温的特殊处理也是有效分离磁性信息的方法。比如，在低温对样品施加 SIRM，之后升温解阻。*Banerjee et al.* [1993] 借助解阻过程的特征定量评估了 SP 成分的含量。利用 SP+SD 与 MD 磁铁矿在低温不同的特点，*Liu et al.* [2004d]在以 SP+SD 信号为主的背景中分离出了 MD 磁铁矿的 Verwey 转换信号。针铁矿的矫顽力大，交变退磁方法难以将其携带的剩磁完全清洗，但在 150 ℃进行加热处理可以有效退磁。磁赤铁矿和磁铁矿的热稳定性有差异，成土作用成因的纳米级磁赤铁矿>300 ℃时会转换成赤铁矿。依据这个原理，土壤样品 300℃附近的磁化强度或磁化率的下降程度可以用来评估磁赤铁矿的含量[*Deng et al.*, 2001]。

不管是物理分离，化学分离还是变温处理，都会破坏样品。相反，借助数学方法对常规磁学测量数据加以处理，可以无损地分解信息。比如样品的矫顽力谱可以通过拟合 IRM 获得曲线而获得[*Robertson and France*, 1994; *Kruiver et al.*, 2001; *Heslop et al.*, 2002; *Egli et al.*, 2004a, b, c]。高矫顽力成分（几百 mT 至几 T 量级）通常是赤铁矿或针铁矿引起。尽管由于铝替代的原因，针铁矿尼尔温度低于室温，通常不携带剩磁，但是若要进一步区分二者的贡献，可以将

样品加热（>150 ℃）进行高温 IRM 测量。总之，结合多种方法可以减少解释的不确定性。不过仅依靠室温 IRM 数据也能够较准确地分离样品中的各个组分。*Egli* [2004a, b, c]介绍了具体的原理、实验过程以及实例。*Heslop and Dillon* [2007]提出端元模型，基于一系列样品的 IRM 获得曲线来分离各组分信息。两种方法都依赖各磁性组分的剩磁线性可加这一假设。分解海洋沉积物的 IRM 获得曲线，可以定量分离其中风成、河流相以及生物成因的组分，所以在研究样品所蕴含的环境信息的问题上被广泛应用[*e.g.*, *Köhler et al.*, 2008; *Roberts et al.*, 2011b; *Just et al.*, 2012]。

磁滞回线反映的同样是样品中各种磁性矿物的综合信息，解释磁滞回线数据的一种经典方法是把测量数据表示在 Day 图上[*Day et al.*, 1977]。Day 图以 B_{cr}/B_c 为横轴 M_r/M_s 为纵轴，已知不同磁畴状态的磁铁矿在 Day 图上位于不同区域，以此为参考可以根据样品数据所在区域来判断样品中磁性矿物的磁畴状态。但实际上，尤其当样品为混合矿物时，Day 图给出的信息是模棱两可的，因此饱受争议。尽管有人提出其它方法替代 Day 图[*e.g., Tauxe et al.*, 2002]，然而由于 Day 图已在岩石磁学和环境磁学领域被广泛使用，有人提出基于 Day 图的分离信息的方法，试图提高 Day 图解释的准确性。*Heslop and Roberts* [2012a, b]应用端元分解法来区分两种混合物的 Day 图。*Dunlop* [2002a, b]详细地介绍了二元混合物在 Day 图上的性质，但 *Heslop and Roberts* [2012a]介绍的方法更有利于定量地分离混合样品信息。不过，天然样品中的混合组分通常比二元混合复杂，因此 *Heslop and Roberts* [2012b]将方法改进为适用于多种组分。如同 IRM 分解法，分解磁滞回线数据以及其他非磁学测量数据也主要依靠数学方法，都将有助于定量化研究环境问题。

另外一种磁滞测量可以提供更丰富的信息。*Pike et al.* [1999] 和 *Roberts et al.* [2000] 介绍了通过测量一阶反转曲线(FORCs) [参见 *Mayergoyz*, 1986]来获得 FORC 图，显示出磁性矿物的矫顽力分布以及磁性颗粒间的磁相互作用。目前，越来越丰富的研究实例使得人们对 FORC 图的理解更加透彻[e.g., *Roberts et al.*, 2000; 2006; *Pike et al*., 2001a, b; *Muxworthy et al.*, 2005; *Yamazaki*, 2009; *Egli et al.*, 2010]。不过 FORC 图的应用仍以定性为主，定量分解不同组分的 FORC 信号的方法则是发展趋势。

穆斯堡尔谱，扫描电镜(SEM)，透射电镜(TEM)，X 射线衍射(XRD)以及漫反射光谱(DRS)等非磁学手段也能有效估计铁氧化的含量。比如 DRS 数据也可以通过分离端元来定量地使用[*Heslop et al.*, 2007]。自然样品的复杂性意味着如果研究者要准确地识别其中的磁性矿物的种类与含量进而研究其环境意义，需要在准确理解样品的磁学性质（固有属性如 T_C 和 T_V，非固有属性如矫顽力）的基础上辅助以适当的非磁学手段。

文献速递

1. 全球极热时期鱼类产量的扩张

翻译人：仲义 zhongy@sustech.edu.cn

Britten G L, Siber E C. ***Enhanced fish production during a period of extreme global warmth*** *[J] Nature Communication, 2020, 11(1), 5135.*

https://doi.org/10.1038/s41467-020-19000-8

摘要：海洋生态模型预测人类世时期海洋变暖会导致鱼类产量大幅度减少，但是在更长时间尺度上鱼类产量变化是否与温度的关系仍然不清楚。作者报告了在全球极度温暖的古近纪早期（62-46 百万年前），海洋温度与底栖的鱼类产量存在正向非线性关系。利用数据控制模型，作者发现，温度驱动的营养转移效率（产量超过营养水平的部分）和初级生产力的增加可以解释鱼类产量的增加，而捕食者-被捕食者相互作用的变化则不行。这些数据对来自地质记录中的上营养层过程提供了新的见解，表明长期变暖可能是导致亚热带远洋生态系统中更高产的食物网。

ABSTRACT: Marine ecosystem models predict a decline in fish production with anthropogenic ocean warming, but how fish production equilibrates to warming on longer timescales is unclear. We report a positive nonlinear correlation between ocean temperature and pelagic fish production during the extreme global warmth of the Early Paleogene Period (62-46 million years ago [Ma]). Using data-constrained modeling, we find that temperature-driven increases in trophic transfer efficiency (the fraction of production passed up trophic levels and primary production can account for the observed increase in fish production, while changes in predator-prey interactions cannot. These data provide new insight into uppertrophic-level processes constrained from the geological record, suggesting that long-term warming may support more productive food webs in subtropical pelagic ecosystems.

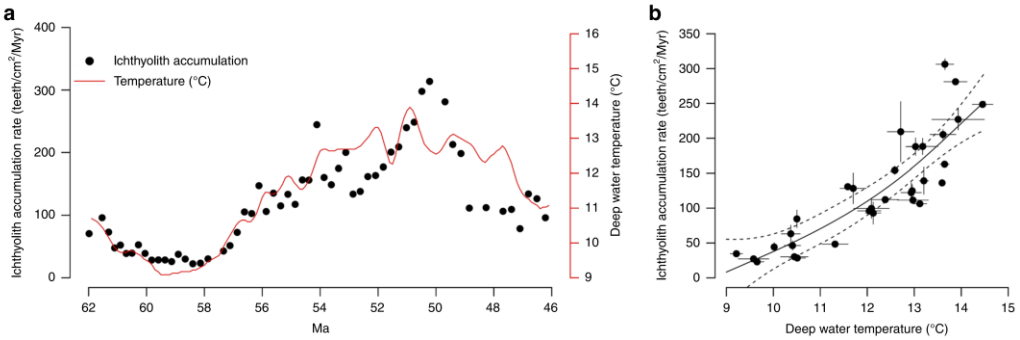

Figure 1. Correlation between fish production and temperature 62–46 Ma. a Observed total ichthyolith accumulation rate (black dots) and paleoceanographic temperature reconstruction derived from $\delta^{18}O$ (red line; ref. 41). b Nonlinear regression between total ichthyolith accumulation rate and paleoceanographic temperature, binned by half Myr time intervals. Black dots give the half Myr-binned means for total ichthyolith accumulation rate and temperature, solid lines around the dots give the sample standard deviation. The solid black curve gives the mean regression and dashed black curves givebthe 95% confidence interval for the regression (n = 32). Source data for (b) are provided as a Source Data file.

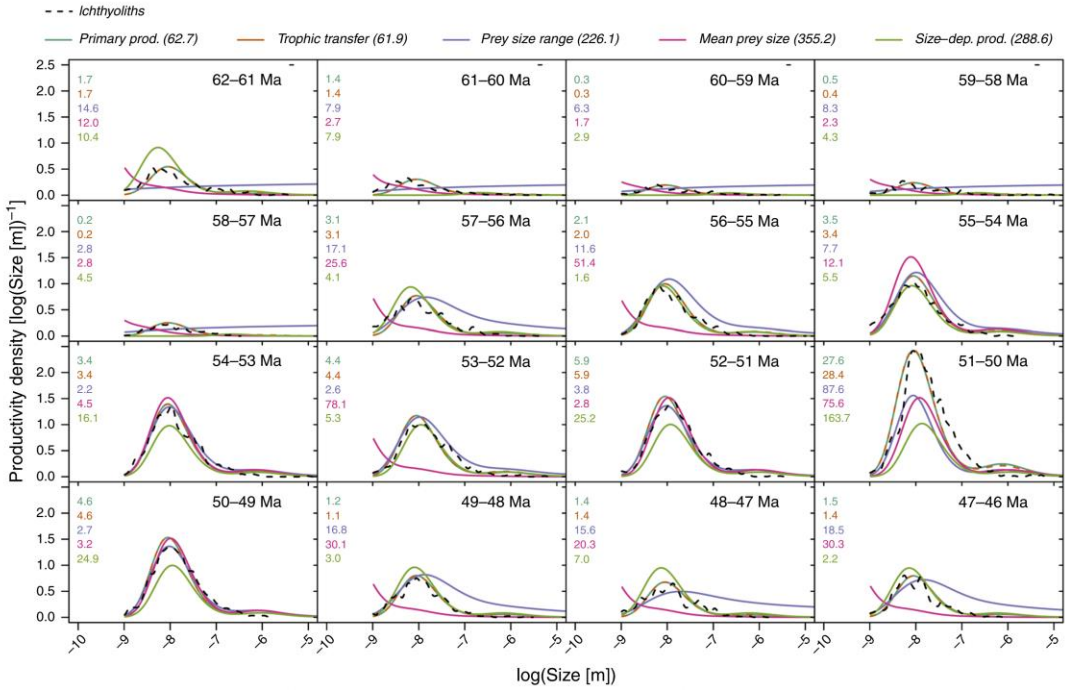

Figure 2. Time series and model fits for the ichthyolith size distributions. Ichthyolith observations (dashed black line) are binned by Myr increments. Model fits are shown for the time-varying primary production model with constant size-productivity scaling (blue), trophic transfer efficiency (orange; shown dashed in the figure due to overlap with the primary production model), prey size range (purple), mean prey size (red), and time-varying primary production with size-dependent scaling (green). The RMSE computed for each Myr bin is displayed in the upper left corner with the same color code and order. The total RMSE across time is given in the top legend in brack.

2. 海洋浮游生物灭绝临界值响应新近纪气候变化

翻译人：蒋晓东 jiangxd@sustech.edu.cn

Trubovitz S, Lazarus D, Renaudie J et al. ***Marine plankton show threshold extinction response to Neogene climate change****[J]. Nature Communications, 2020, 11:5069.*

https://doi.org/10.1038/s41467-020-18879-7

摘要：气候变化被认为触发了海洋浮游生物种类的地理分布。然而对于这些种群是否能找到最佳的栖息地或者面对灭绝仍然不清楚。本研究发现在晚新近纪变冷时段在高纬度地区一种重要的浮游动物（放射虫）种群丰度急剧降低，并预示着种群的重新组织。大多数（71%）受影响的种群并未迁移至温暖的低纬度地区而是直接灭绝了。这意味着一些浮游生物在全球尺度并不能追寻最佳温度，这一结果与生态模型一致。相反，一旦环境变化超越了临界值这些种群将经受重组并且灭绝。这一模式预示着将来高纬度地区放射虫多样性的显著降低，这一结果可能会逐级影响海洋生物的食物链和碳循环。

ABSTRACT: Ongoing climate change is predicted to trigger major shifts in the geographic distribution of marine plankton species. However, it remains unclear whether species will successfully track optimal habitats to new regions, or face extinction. Here we show that one significant zooplankton group, the radiolaria, underwent a severe decline in high latitude species richness presaged by ecologic reorganization during the late Neogene, a time of amplified polar cooling. We find that the majority (71%) of affected species did not relocate to the warmer low latitudes, but went extinct. This indicates that some plankton species cannot track optimal temperatures on a global scale as assumed by ecologic models; instead, assemblages undergo restructuring and extinction once local environmental thresholds are exceeded. This pattern forewarns profound diversity loss of high latitude radiolaria in the near future, which may have cascading effects on the ocean food web and carbon cycle.

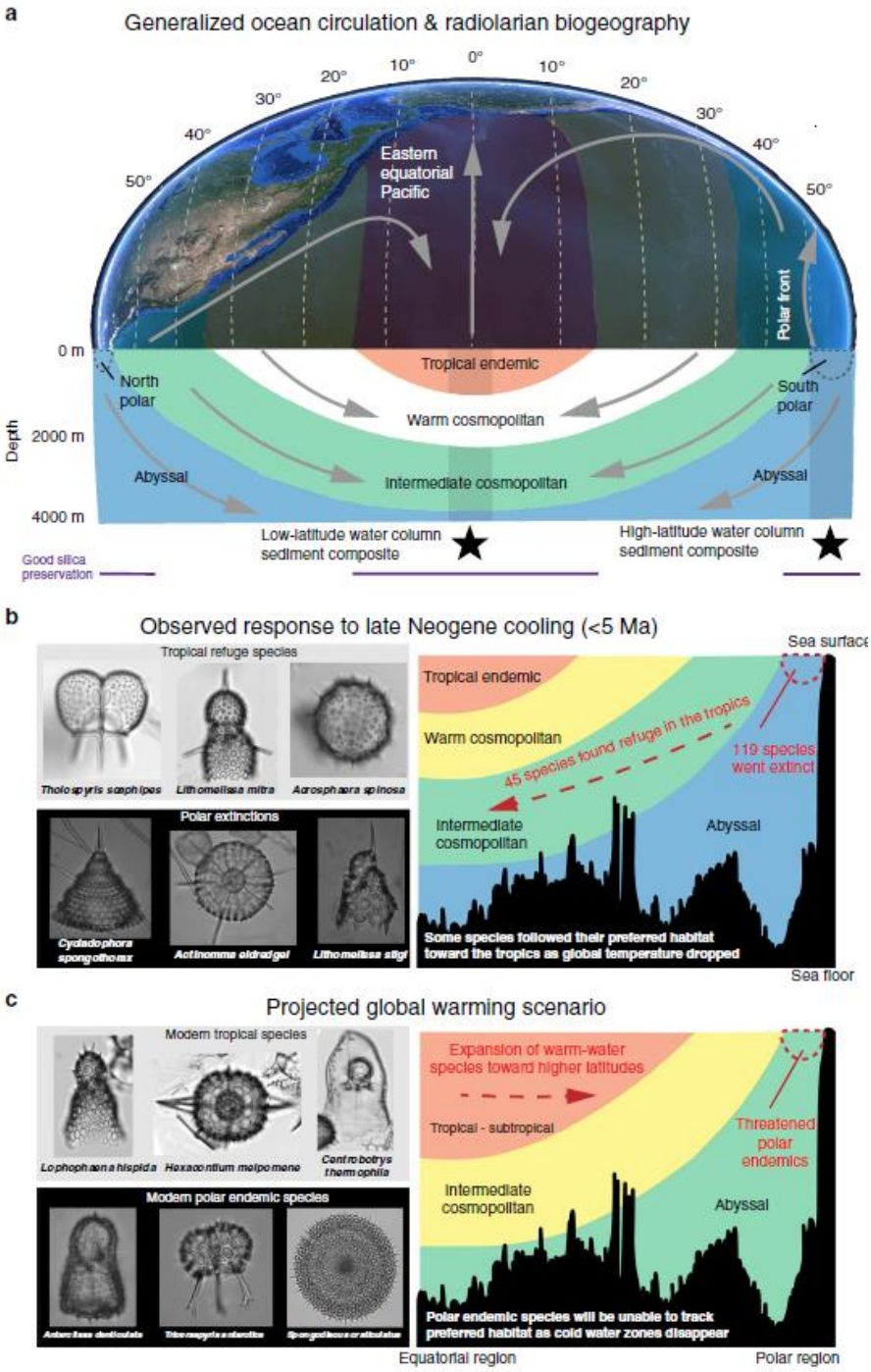

Figure 1. Radiolarian biogeography with observed and predicted responses to temperature change. a Illustrates generalized radiolarian provinces and their relationship to water mass temperature (warm versus cool color shading) and circulation (gray arrows). Due to high-latitude water mass submergence under warm, stratified waters in lower latitudes, radiolarian species occupy habitats at multiple latitudes, and depths throughout the world oceans. Thus, marine sediments from the tropics reflect a composite of several vertically stacked faunal assemblages, some of which are contiguous with higher latitude surface assemblages. Sediments beneath polar waters include cosmopolitan deep-water radiolarians, as well as high-latitude endemic surface water species. Stars in (a) indicate the latitudes sampled for this study, and the gray bars highlight the radiolarian assemblages included

in each sedimentary composite. The horizontal purple bars indicate latitudes known for good radiolarian (silica) preservation, based on surface sediment composition. Our data show that some species were extirpated from high latitudes but persisted in the tropics during the late Neogene, either by migration or range restriction (b). With predicted global warming, modern Southern Ocean species will not be able to use migration or range contraction to escape environmental stressors, because their preferred cold-water habitats are disappearing from the globe (c). However, tropical endemic species may expand their ranges toward midlatitudes. The color polygons in all three panels represent generalized radiolarian biogeographic provinces, as well as their relative water mass temperatures (cooler colors indicate cooler temperatures, and vice versa). Globe image adapted from NASA Blue Marble: Next Generation imagery. Ocean floor bathymetry from Google EarthTM seafloor elevation profile (5°N–74°S, at 120°W).

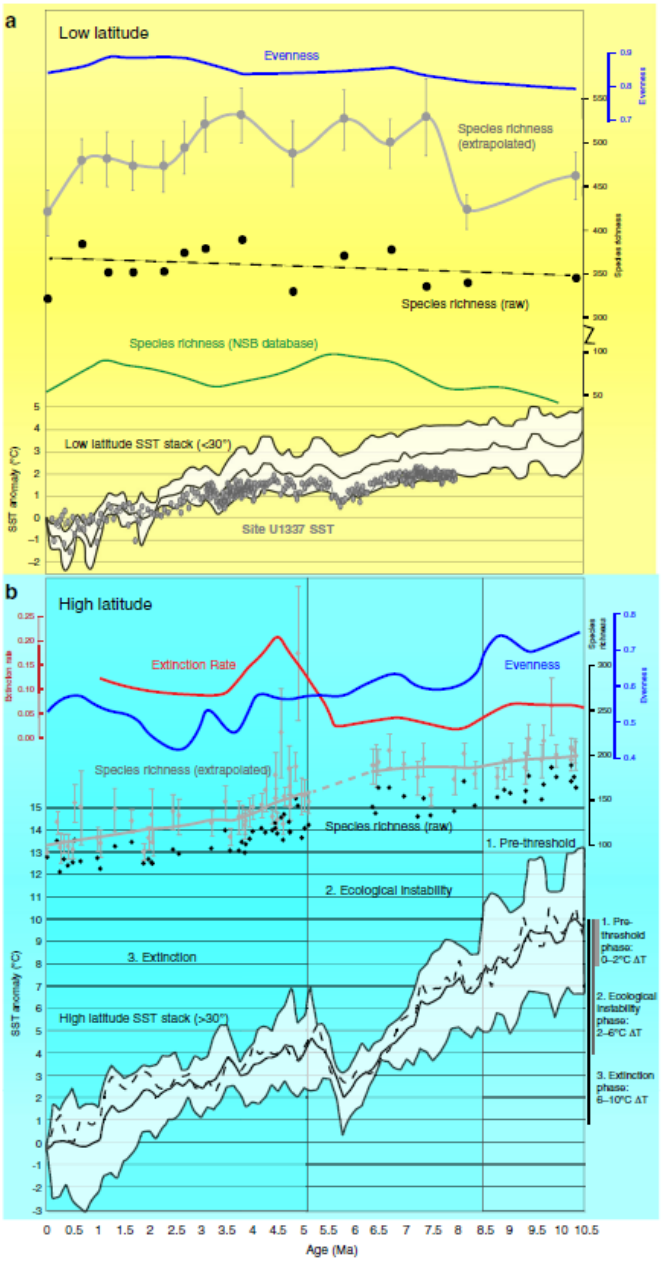

Figure 2. Radiolarian evolution and sea surface temperature (SST) over the last 10 million years. In

both panels, black points indicate raw species richness observed in each sample. Extrapolated species richness (asymptotic diversity estimates) are shown in gray. Error bars indicate the mean (center) ± standard error, based on 500 bootstrap replicates. Extrapolation was performed using the R package iNext66 (Hill numbers of order q = 0), and is based on sample completeness34. A lowess smoother (span =0.33) is applied to the lower panel to aid with visualization; a dashed line is used across the data gap. Evenness (Pielou equitability index38) is plotted in blue, and boundary-crosser extinction rate70 is plotted in red (most recent time bin removed due to edge effect, see "Methods"). The green line in (a) refers to tropical Pacific radiolarian diversity recorded in the Neptune Sandbox Berlin (NSB) database37, which includes data from previous deep-sea drilling research (note broken scale). Southern Ocean radiolarian data were obtained from9 and re-analyzed for this study using updated age models in NSB. Temperature data are re-plotted from, and are based on alkenone biomarker proxy reconstructions. In (a) the SST anomaly curve indicates mean tropical SST over time and one standard deviation from the mean, as reported in8. The gray data points show SST data from Site U1337 only29. In (b), the black line indicates the mean SST for compiled northern hemisphere and southern hemisphere mid and high latitudes8. The dashed line indicates the median value among these datasets, and the envelope refers to the maximum and minimum average temperatures among these datasets. Due to some uncertainty in Southern Ocean age models, only broad patterns on the scale of ~1 million year (Ma) should be considered in (b), rather than precise temporal correlations between radiolarian evolution and temperature. The gap in sampling between ~5 and 6.5 Ma shown in (b) is due to a regional sedimentation hiatus and high age model uncertainty of this specific time interval at the Southern Ocean sites. Different shades of blue background in (b) refer to phases of Southern Ocean radiolarian response (see text).

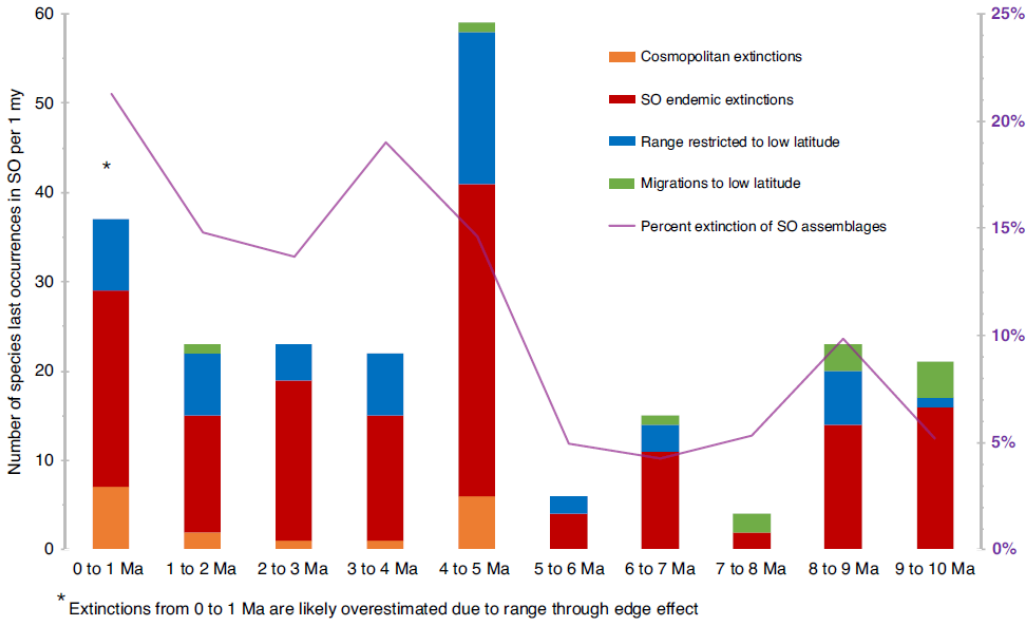

Figure 3. Fate of species that disappeared from Southern Ocean assemblages during the late Neogene. Last occurrence datums of Southern Ocean (SO) species were compiled into 1 million-year bins, after each species was ranged through its first and last occurrence in the dataset (see "Methods"). Last occurrences were cross-checked against the low-latitude range-through species dataset, to determine whether the SO species were extirpated to warmer climates or went globally

extinct. Warm colors represent extinctions and cool colors represent extirpations. Red bars = number of endemic SO species that became globally extinct; orange bars= cosmopolitan species that went extinct; blue bars= cosmopolitan species that restricted their range to the low latitudes; and green bars =endemic SO species that relocated from the SO to the low latitudes (migrations). The purple line indicates the percentage of the SO species assemblage that suffered extinction in each time bin (species that did not persist to the next time bin in the SO, nor were extirpated to low latitudes via migration or range restriction; see "Methods"). Overall, extinction was the main cause of SO diversity decline throughout the study interval. Migration was the least common outcome for species that disappeared from the SO. The highest extinction rate occurred between 5 and 4 million years (Ma), but high extinction continued into the Late Pliocene and Pleistocene. From 0 to 1 Ma, the number and percentage of extinctions may be an overestimate, because it is not possible to range-through species in the most recent time bin (see "Methods"). Therefore, some species may appear to have gone extinct, but were actually just too rare to be observed in the most recent samples. The data used in this figure are reported in Supplementary Data 3. A list of low-latitude species from the eastern equatorial Pacific is given in Supplementary Data

3. 二氧化碳在减弱的卡洛琳地幔柱火山活动中扮演重要角色的证据

翻译人：冯婉仪 fengwy@sustech.edu.cn

Zhang G L, Wang S, Zhang J. ***Evidence for the essential role of CO_2 in the volcanism of the waning Caroline mantle plume****[J]. Geochimica et Cosmochimica Acta, 2020,290: 391-407. https://doi.org/10.1016/j.gca.2020.09.018*

摘要：来源于地球深部的地幔柱为地球内部和表面之间的碳提供了联系。含 CO_2 的地幔发生低程度部分熔融被认为能产生深部地幔中的碳酸盐熔体，但碳酸盐熔体在现代海洋环境中很少发现，而且原始碳酸盐化硅酸盐熔体在地幔柱火山作用中的作用尚不清楚。由于地幔发生低程度熔融倾向于生成富含 CO_2 的熔体，所以本文以全岩主量元素、微量元素、Sr-Nd-Pb-Hf 同位素和高精度的矿物原位成分为基础，研究了一套来自由减弱的卡罗琳地幔柱形成的波恩佩岛的火山岩。我们证明了这些火山岩的矿物学和地球化学特征与高 MgO 的原始碳酸盐化硅酸盐熔体的矿物学和地球化学特征一致，例如：它们是目前报导的洋岛玄武岩中最贫 SiO_2 和最富 CaO 的，而且它们富集稀土元素和亏损高场强元素。这些火山岩的 Sr-Nd-Pb-Hf 同位素组成显示出源区是太平洋型亏损地幔和类似富集地幔 II （EM2）的混合。我们发现，在岩浆上升至岩石圈过程中，原始的碳酸盐化硅酸盐熔体经过反应演化和 CO_2 去气作用，演变为典型的洋岛碱性玄武岩，并确定了这些熔体与岩石圈地幔达到平衡后的封闭体系演化阶段。我们认为，减弱的地幔柱发生低程度熔融促进了碳酸盐化硅酸盐熔体的火山作用，并且在上覆厚岩石圈地幔中，碳酸盐化硅酸盐熔体逐渐演变为典型的洋岛碱性玄武岩。橄榄石中异常低的 Ca 和 Mn 含量以及 Ca 在橄榄石与熔体之间的分配系数表明，原始岩浆的 CO_2 含量为 11-15 wt.%。这些火山岩中还含有类似夏威夷的高 Ni 橄榄石，我们认为这反映了富辉石岩、贫橄榄石的地幔源区。本文所提出的碳酸盐熔体在岩石圈地幔的反应演化往往导致深部地幔中 CO_2 的损失，并且控制了碳酸盐熔体的命运，这可能解释了大洋板块内部环境中碱性玄武岩广泛存在而碳酸盐熔体罕见的现象。

ABSTRACT: Deep-rooted marine mantle plumes provide a link for carbon between Earth's interior

and its surface. Low-degree partial melting of CO_2-bearing mantle is predicted to produce carbonated melts in the deep mantle, but carbonated melts are rarely found in modern oceanic settings, and the role of primary carbonated silicate melts in mantle-plume volcanism remains unclear. Because low-degree mantle melting tends to generate CO_2-rich melts, we studied a suite of volcanic rocks from Pohnpei Island formed by the waning Caroline mantle plume based on whole-rock major- and trace-element, Sr–Nd–Pb–Hf isotopic, and high-precision in situ mineral compositions. We demonstrate that the mineralogy and geochemistry of these volcanic rocks are consistent with those of high-MgO primary carbonated silicate melts, e.g., they have the most SiO_2-depleted and CaOenriched compositions reported for ocean-island basalts, they are enriched in rare-earth elements and have negative anomalies of high-field-strength-elements. The Sr–Nd–Pb–Hf isotopic compositions of these volcanic rocks exhibit mixing between the Pacific-type depleted mantle and an enriched-mantle II (EM2)-like source. We found that primary carbonated silicate melts were modified to become typical ocean-island alkali basalts through reactive evolution and CO_2 degassing during magma ascent in the lithosphere, and also identified a closed-system stage of evolution after these melts reached equilibrium with the lithospheric mantle. We suggest that low-degree melting of a waning mantle plume facilitates carbonated-silicate-melt volcanism, with the carbonated silicate melts being converted to typical alkali ocean-island basalt in the overlying thick lithospheric mantle. The anomalously low olivine Ca and Mn contents and the Ca partition coefficient between olivine and melt suggest that the primary magmas had a CO_2 content of 11–15 wt.%. These volcanic rocks also contain Hawaii-like high-Ni olivines, which we interpret as reflecting a pyroxenite-rich and olivine-poor mantle source. The proposed reactive evolution of carbonated melts in the lithospheric mantle tends to cause loss of CO_2 in the deep mantle and regulates the fate of carbonated melts, which may explain the widespread occurrence of alkali basalts and the rarity of carbonated melts in intraoceanic-plate settings.

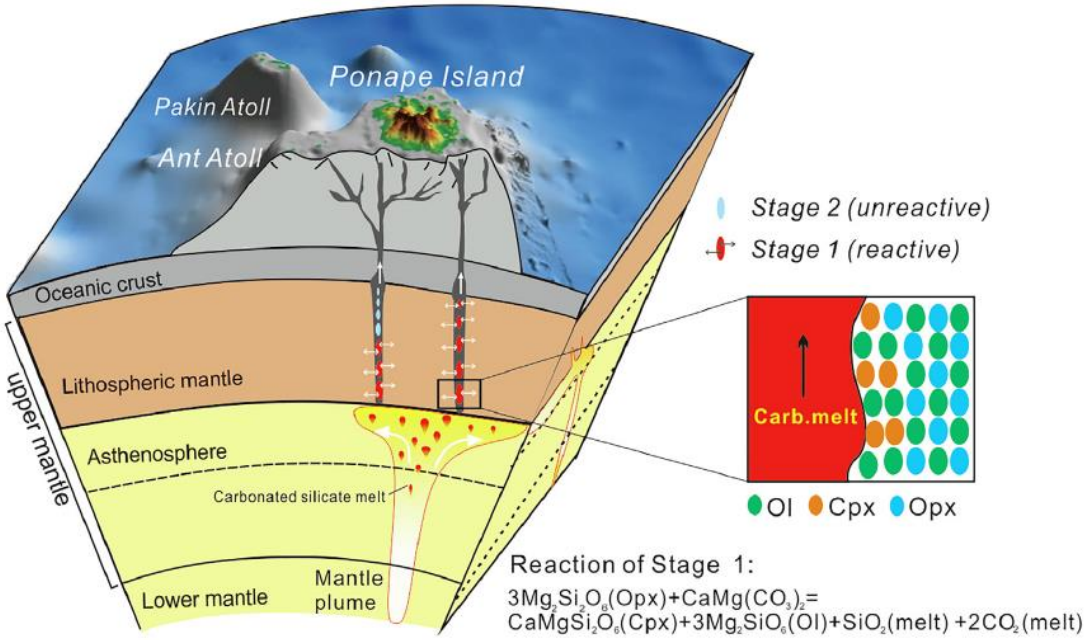

Figure 1. Sketch model for the evolution of carbonated silicate melts in the lithospheric mantle.

4. 冲绳海槽南部边缘的高密度探测揭示出胚胎裂谷区

翻译人:李园洁 liyj3@sustech.edu.cn

Misawa A, Sato M, Furuyama S et al. ***Embryonic rifting zone revealed by a high-density survey on the southern margin of the southern Okinawa Trough*** *[J]. Geophysical Research Letters, 2020. 47, e2020GL090161. https://doi. org/10.1029/2020GL090161*

摘要：冲绳海槽南部的 Ishigaki-Jima 岛北部近海可提供机会研究弧后系统的裂解过程。本文作者综合这个区域地质和高密度地球物理探测结果，识别出一个由正断层界定的地堑，其在冲绳海槽南部的偏轴 ENE-WSW 方向上延伸了约 59 km。地堑内存在具有活跃热液活动和相关侵入性结构的海底火山。地堑中及其周围的磁异常和地震活动数据表明，存在着相对较浅的岩浆作为热源。地堑内及其周围发现的所有特征都表明冲绳海槽南部正在积极裂解。

ABSTRACT：Offshore northern Ishigaki-Jima Island, in the southern Okinawa Trough, offers outstanding opportunities to explore the rifting stage of a backarc system. We report the results of integrated marine geological and geophysical surveys with high-density survey lines in this area. We identify a graben bounded by normal faults and extending approximately 59 km in an ENE-WSW direction off-axis of the southern Okinawa Trough. Submarine volcanoes with active hydrothermalism and associated intrusive structures lie in the graben. Magnetic anomaly and seismicity data in and around the graben suggest the presence of relatively shallow magma acting as a heat source. All features identified in and around the graben suggest active rifting in the southern Okinawa Trough.

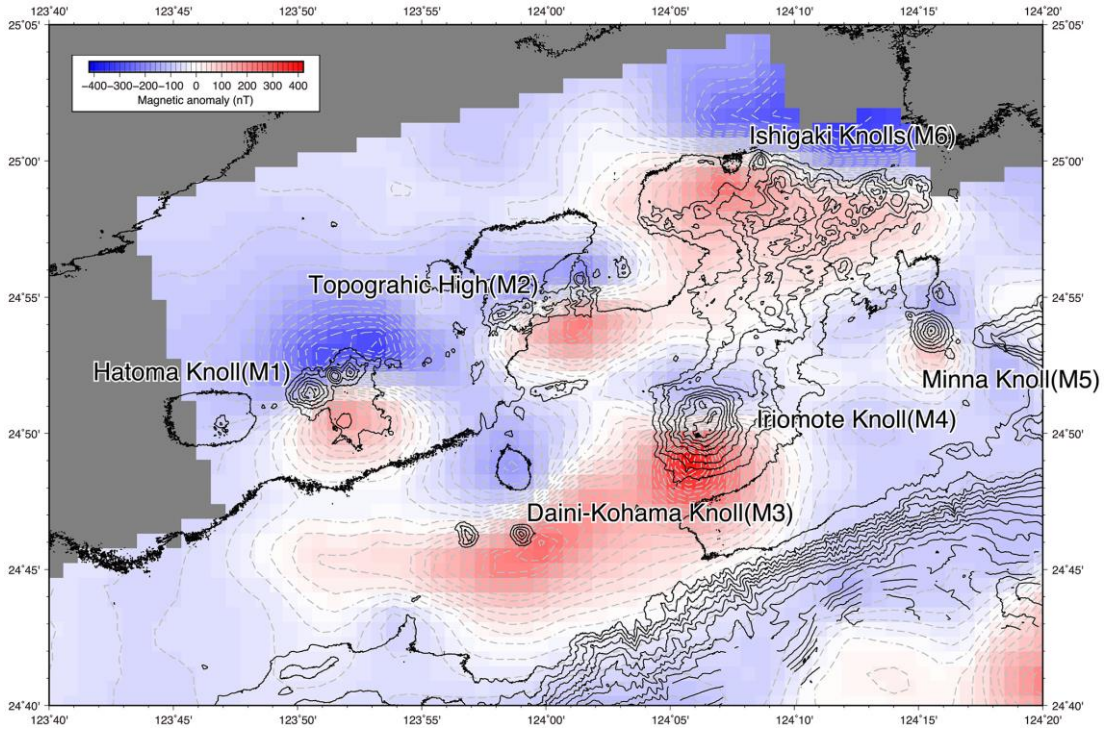

Figure 1. Magnetic anomaly map offshore northern Ishigaki-Jima Island. The magnetic anomaly map grid interval is 1 km, and the contour interval is 20 nT. Dipole anomalies lie around the knolls, which are submarine volcanoes. They are characterized by a narrow interval between the positive and negative dipole anomalies. Bathymetry contours are shown as black lines. The bathymetry contour interval is 100 m.

5. 美国西部全新世古气候变化：年代学在识别模式和驱动因素中的重要性

翻译人：柳加波

Zimmerman S R H, Wahl D B. ***Holocene paleoclimate change in the western US: The importance of chronology in discerning patterns and drivers*** *[J]. Quaternary Science Reviews, 2020, 246: 106487. https://doi.org/10.1016/j.quascirev.2020.106487*

摘要：湖泊沉积物是重建古环境随时间变化的强大档案库。重建湖泊的水位、化学、生物和水文状况以及周围植被能够提供局部的和区域的详细古气候信息。尤其是位于干旱的美国西部，目前我们对百年至千年尺度上气候变化的了解都来自于这种基于沉积物的环境重建。渴望对未来环境状况的可靠、准确预测是古气候科学以及当前关注全新世亚百年尺度气候重建的主要动力。区域综合越来越多地寻求识别与现代观测（季节，年际，十年年代等）相似的天气尺度模式，或与气候模拟的结果进行比较。但是，对现有记录（尤其是超过 20 岁的记录）的年龄控制通常仅能实现千年尺度的解释。本文，我们评估了来自加利福尼亚大盆地和西南沙漠的湖泊和草甸的 84 条已发布和未发布记录的年龄控制，并使用贝叶斯模型评估了 42 条最佳记录的 95%不确定性范围。在晚全新世，42 条记录中约有一半具有小于 400 年的平均不确定性范围。但是，高精度的年龄控制对于年轻记录尤为重要，因为该记录可用于准确了解代用指标对已知气候变化的响应。在中全新世，记录的平均不确定度在 400 至> 800 年之间，早期全新世的记录的平均不确定度在 600 至> 1400 年之间。我们发现，控制年代模型不确定性的最大因素是年代点的密度。每千年至少两个年代点是最理想的，并且在研究的开始阶段获得“查找范围”的年代，能够更好得预测一个充分的年代模型所需要的年代点总数。这样的密度避免了通常所观察到的在年龄控制点之间出现的不确定性峰值的现象。对于代用指标偏移相关的不确定性分析表明，超过一半是大于 400 年的。在大多数情况下，目前如此大的误差不能够提供亚百年尺度上的解释。但是，不断增加的定年密度、有限资金的战略性使用（包括在提案阶段至少 2 个定年点/千年的预算）、贝叶斯年龄深度模型的使用和年代误差的严格评估，将会在更精细的时间尺度上揭示过去的气候变化，从而加深我们对美国西部气候变化的全球和区域驱动力的理解。

ABSTRACT: Sediment in lakes and meadows forms a powerful archive that can be used to reconstruct environmental change through time. Reconstructions of lake level, of chemical, biological, and hydrological conditions, and of surrounding vegetation provide detailed information about past climate conditions, both locally and regionally. Indeed, most of our current knowledge of centennial- to millennial-scale climate variability in the arid western United States, where information about past hydroclimate is particularly important, comes from such sediment-based reconstructions. The pressing need for robust, precise predictions of future conditions is a significant motivation for paleoclimate science, and current research questions frequently require Holocene reconstructions to be resolved at sub-centennial timescales. Increasingly, regional syntheses seek to identify synoptic-scale patterns similar to those defined from modern observations (seasonal, interannual, multi-decadal, etc.) or to compare with the output of climate model simulations. However, the age control on existing records, especially those more than about 20 years old, is often sufficient only for millennial-scale interpretation. Here we assess the age control for 84 published and unpublished records from lakes and meadows in the Great Basin, California, and desert southwest, and use Bayesian modeling to evaluate the 95% uncertainty ranges for the 42 best-dated records. In the Late Holocene, about half of the 42 records have <400-year mean uncertainty ranges; however, high-precision age control is especially critical for young records, used to develop an accurate understanding of a proxy's response to known climate variations. In the Middle Holocene, records vary from 400 to >800-year mean uncertainty and records of the Early Holocene have 600- to >1400-year mean uncertainty ranges. We find that the largest control on modeled uncertainties is dating density, with at least 2 dates/kyr being optimal and suggest obtaining "range-finder" dates at the onset of a study to better predict the total number of dates needed for an adequate age model. Such a density avoids a commonly observed phenomenon of significant peaks in uncertainty arising in gaps between age control points. Analysis of the uncertainties associated with proxy shifts reveal that more than half are >400 years. Although such large uncertainties currently prevent sub-centennial interpretations in most cases, increased dating density, strategic use of limited funds (including budgeting for a 2 date/kyr minimum at the proposal stage), construction of age-depth models with Bayesian methods, and critical evaluation of chronological uncertainty will shed light

on past climate variability at finer timescales, enhancing our understanding of global and regional drivers of western U.S. climate.

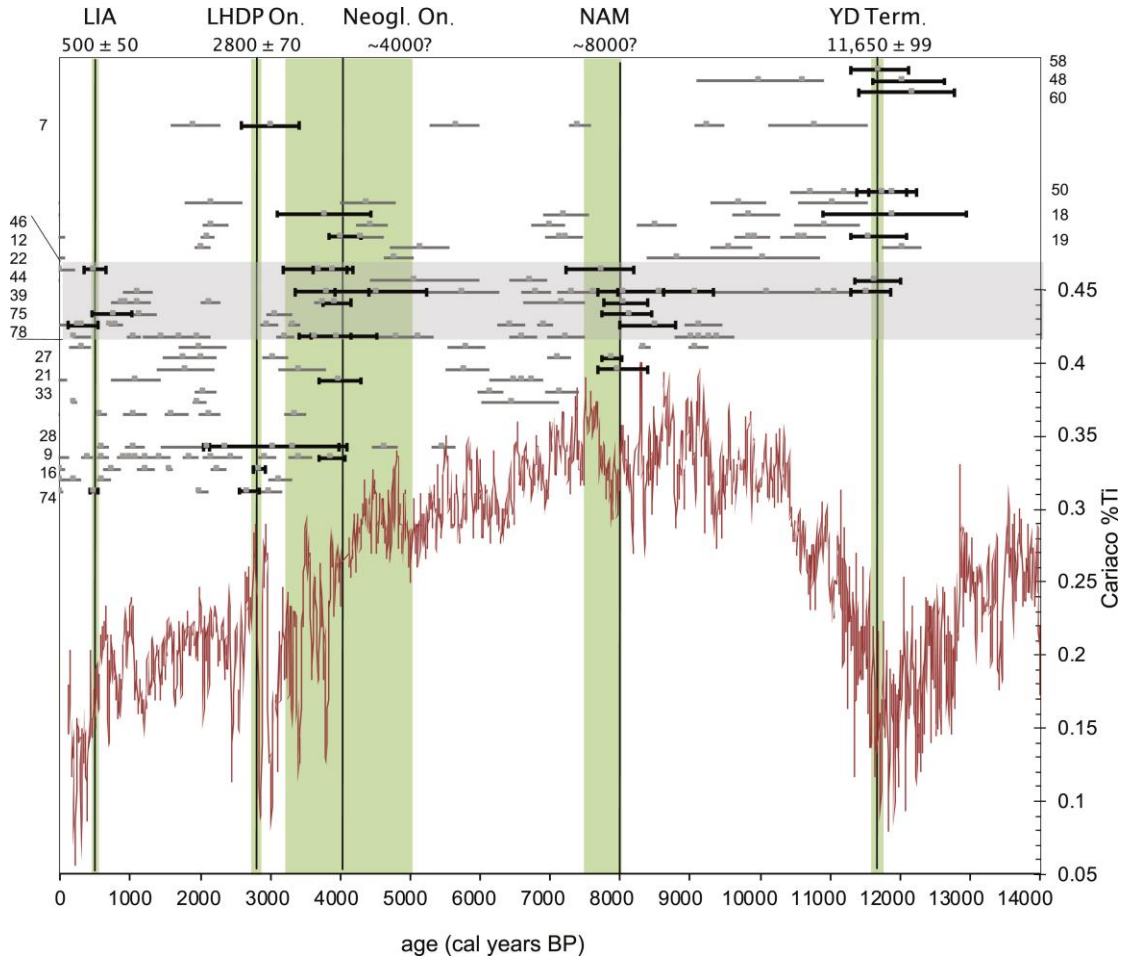

Figure 1. Illustration of the overlap between the ages of the zone/event boundaries in each record and the times of major paleoclimate change in the western United States. Pink curve below is the Cariaco Basin record of the ITCZ, and the green bands are as described for Fig. 2. Boundaries whose age-uncertainty window overlaps the year of the shift are shown in black; corresponding site numbers from Table 1 are listed on the y axes. Gray bars indicate boundaries that do not overlap temporally with the single year; some do overlap with the green uncertainty boxes (see section 6 for discussion). Many of these may be local changes in environment or ecology, but a pattern of changes overlapping the major climate shifts would indicate a larger-scale driver of regional change. Note that not all of the boundaries identified are shown, as some are younger than 1950 CE (0 cal y r BP).

6. 菲律宾海板块 Izu–Bonin 弧与太平洋板块 Ogasawara 高原碰撞带 Hahajima 海山东部斜坡碳酸盐岩沉积的构造意义

翻译人：刘伟 inewway@163.com

Miyata J, Takayanagi H, Ishigaki A et al. ***Tectonic implications of carbonate deposits on the eastern slope of the Hahajima Seamount in the collision zone between the Izu–Bonin Arc on the Philippine Sea Plate and the Ogasawara Plateau on the Pacific Plate*** *[J]. Island Arc, 2020. https://doi.org/10.1111/iar.12368*

摘要：Hahajima 海山位于 Izu–Bonin 弧和 Mariana 弧前斜坡之间，是菲律宾海板块和太平洋板块 Ogasawara 高原的交汇处。尽管之前进行了大量的研究，但 Hahajima 海山的起源仍然存在争议。本文通过对从海山东坡采集的浅水碳酸盐岩的沉积学和年代分析，确定了其成因。碳酸盐岩以浮石为主，其中有许多软体动物。砾石大小的生物碎屑包括软体动物(例如栉水母和甲壳类)、本地钙质棘和少量珊瑚。砂粒大小的成分包括底栖有孔虫类的生物碎屑和粗枝藻的生物碎屑，以及无骨架的内碎屑和似球粒，没有鲕粒。大部分生物碎屑被生物侵蚀，包裹有泥晶包膜。样品的 Sr 同位素年龄分为两个范围: 140.3 Ma 或 118.3-113.2 Ma 和 86.5-77.2 Ma。Hahajima 海山的浅水碳酸盐岩在岩性和 Sr 同位素年龄上与 Izu–Bonin 海沟一侧的 Ogasawara 高原相似。这表明，Hahajima 海山东坡浅水碳酸盐岩并非原地沉积，而是起源于 Ogasawara 高原。因此，该海山的东段可以解释为一个增生楔。

ABSTRACT: The Hahajima Seamount is located at the junction between the Izu–Bonin and Mariana forearc slopes in the northwest Pacific Ocean, and between the Philippine Sea Plate and the Ogasawara Plateau on the Pacific Plate. Despite numerous previous studies, the origin of the Hahajima Seamount remains controversial. Here we constrain its origin based on sedimentological and chronological analyses of shallow-water carbonates collected from the eastern slope of the seamount. The carbonates are dominated by floatstones with numerous mollusks. Gravel-sized bioclasts include mollusks (e.g. nerineids and rudists) and local calcareous spines and minor

amounts of corals. Sand-sized components include bioclasts of benthic foraminifers and dasycladalean algae, and non-skeletal grains of intraclasts and peloids, with no ooids. Most of the bioclasts are bioeroded and coated with micrite envelopes. The Sr isotope ages of the samples fell into two ranges: Berriasian or Aptian (140.3 Ma or 118.3–113.2 Ma, respectively) and Coniacian to Campanian (86.5–77.2 Ma). Shallow-water carbonates on the Hahajima Seamount are similar in lithology and Sr isotope ages to those on the Ogasawara Plateau located to the east, on the opposite side of the Izu–Bonin Trench (i.e. on the Pacific Plate). This indicates that the shallow-water carbonates on the eastern slope of the Hahajima Seamount were not deposited in situ, but instead originated from the Ogasawara Plateau. The eastern section of this seamount can thus be interpreted as an accretionary wedge.

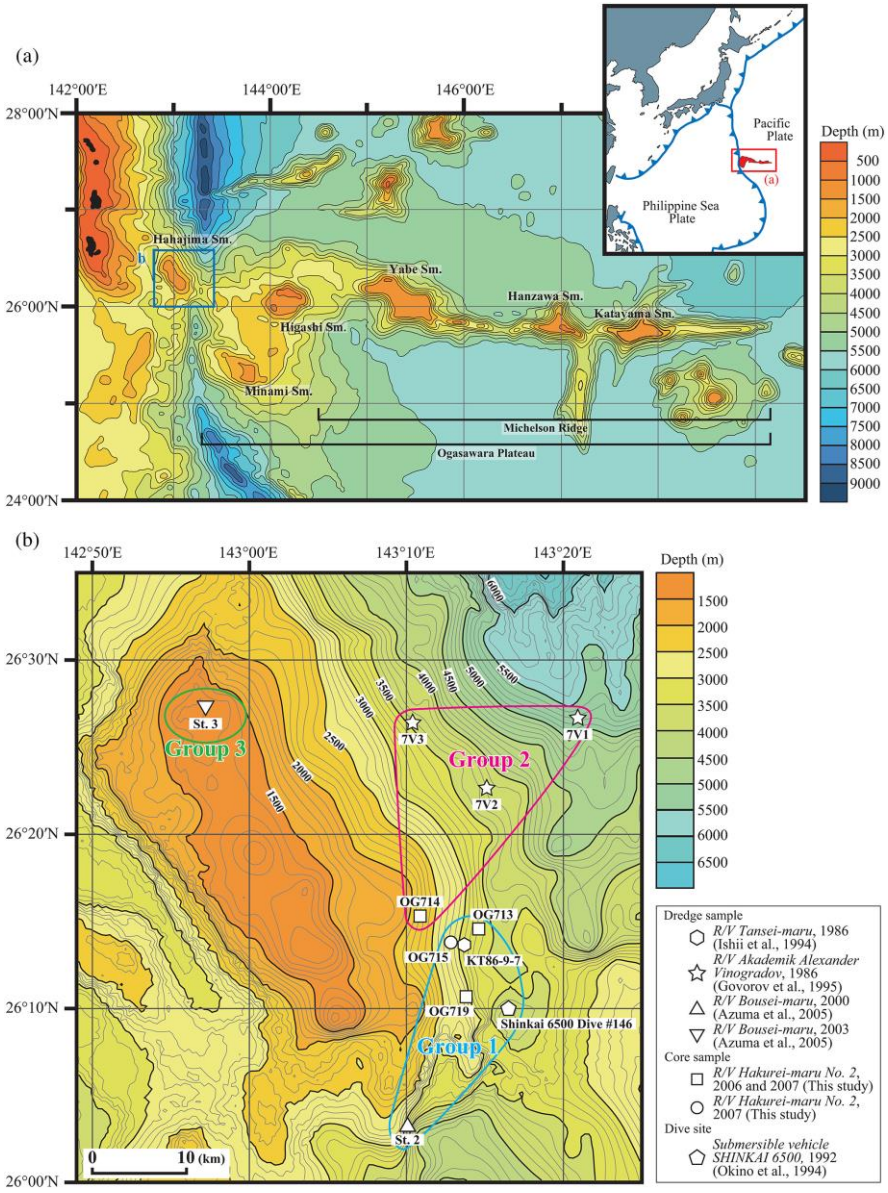

Figure 1. Maps showing the location of the study area, bathymetry, and sample sites. (a) Submarine topography of the Hahajima Seamount and the Ogasawara Plateau. (b) Detailed submarine topography of the Hahajima Seamount. Sampling sites and respective research cruises are shown by group numbers (see Discussion).

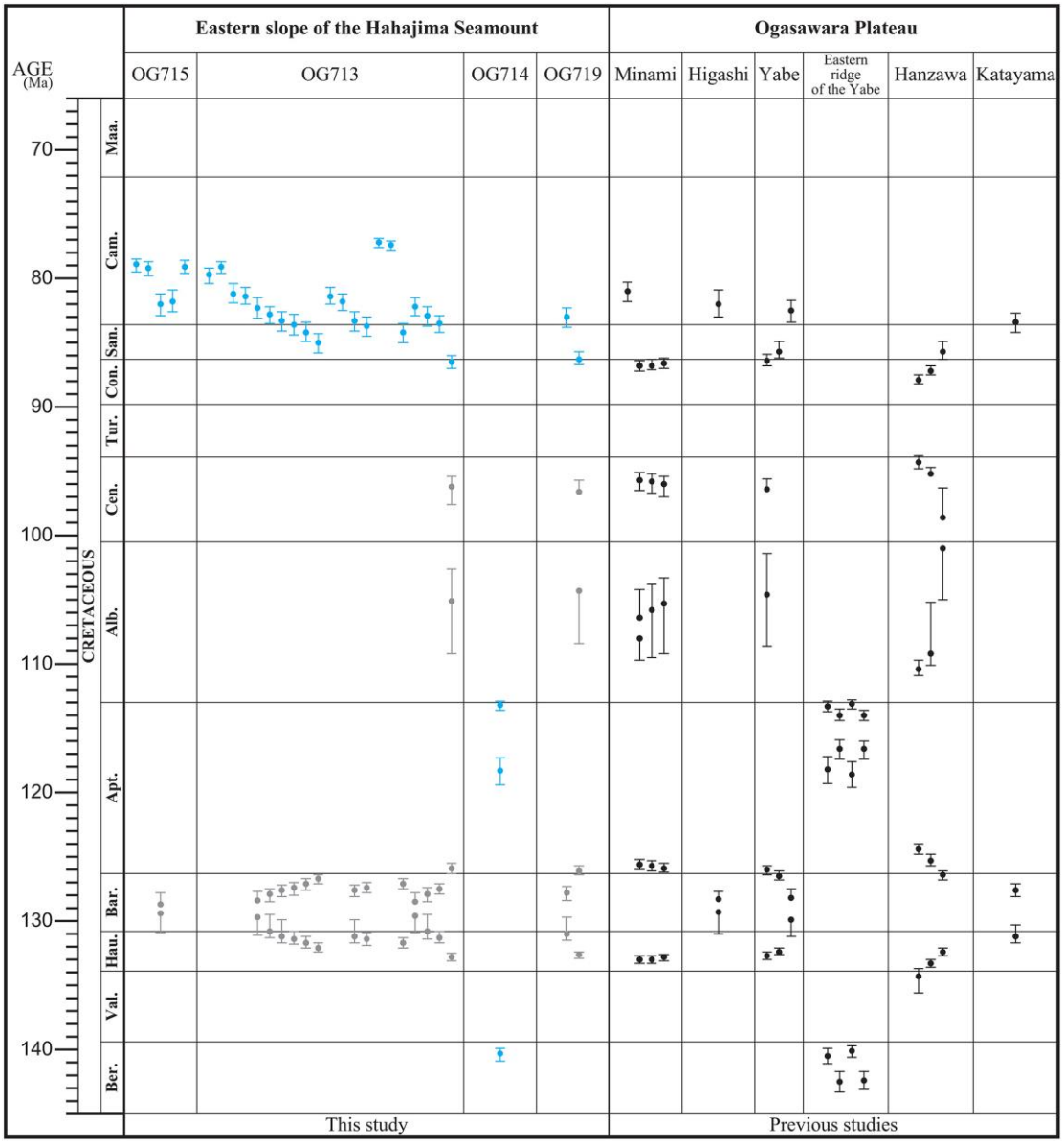

Figure 2. Sr isotope ages of shallow - water carbonates from the Hahajima Seamount and five seamounts on the Ogasawara Plateau. The most plausible ages for the shallow - water carbonates from the Hahajima Seamount are shown in blue. Sr isotope ages of the carbonates from the Minami, Yabe (including the eastern ridge), Hanzawa, and Katayama seamounts (Takayanagi et al., 2007, 2012) were re - calculated using the global calibration curve (McArthur et al., 2012). Although the age of the shallow - water carbonates on the Higashi Seamount was reported as ~ 100 Ma by Nishimura et al. (1994), it was re - calculated as 82.0 Ma

7. 铁锰结壳形成和成岩作用的光谱研究

翻译人：曹伟 11930854@QQ.com

Sutherland K M, Wankel S D, Hein R J et al. ***Spectroscopic insights into ferromanganese crust formation and diagenesis*** *[J]. Geochemistry, Geophysics, Geosystems, 2020. https://doi.org/10.1029/2020GC009074*

摘要：海洋铁锰氧化沉积物，通常被称为海洋的清道夫，其吸附和共沉淀的金属范围广泛，对古环境重建和经济地质学具有重要意义。锰铁氧化沉积所提供的海水化学长期(高达 75 Ma)的近连续记录，提供了许多有关全球海洋和地球表面的历史信息，包括地壳形成、地幔过程、海洋环流和生物地球化学循环。然而，海底铁锰介壳在形成过程中所记录这些地球化学指标的程度，仍然是评估此类记录真实性的一个重要和具有挑战性的因素。在本项研究中，我们使用多种 X 射线技术，包括 micro X-ray fluorescence, bulk and micro X-ray absorption spectroscopy 以及 X-ray powder diffraction 来探测单个铁锰结壳的结构、成分、氧化还原和矿物变化。这些技术揭示了一个由锰（Mn）所控制的介壳生长复杂二维结构，其特征是锰氧化状态随着时间变化在+3.4 到+4.0 之间的动态范围，以及地壳较低磷化部分的重结晶。铁（Fe）在浓度和矿物学方面同样表现出空间复杂性，但缺乏锰的动态氧化范围。金属丰度的微米级测量揭示了微量元素与两种主要氧化物之间的复杂元素关联，这种关联通常无法通过批量分析方法解析。这些发现为沉积作用改变化学和矿物提供了证据，并为铁锰结壳的元素和同位素记录解释提供了重要的地球化学背景。

ABSTRACT: Marine ferromanganese deposits, often called the scavengers of the sea, adsorb and coprecipitate with a wide range of metals of great interest for paleo-environmental reconstructions and economic geology. The long (up to ~75 Ma), near-continuous record of seawater chemistry afforded by ferromanganese deposits offers much historical information about the global ocean and surface earth including crustal processes, mantle processes, ocean circulation, and biogeochemical cycles. The extent to which the ferromanganese deposits hosting these geochemical proxies undergo

diagenesis on the seafloor, however, remains an important and challenging factor in assessing the fidelity of such records. In this study, we employ multiple X-ray techniques including micro X-ray fluorescence, bulk and micro X-ray absorption spectroscopy, and X-ray powder diffraction to probe the structural, compositional, redox, and mineral changes within a single ferromanganese crust. These techniques illuminate a complex two-dimensional structure characterized by crust growth controlled by the availability of manganese (Mn), a dynamic range in Mn oxidation state from +3.4 to +4.0, changes in Mn mineralogy over time, and recrystallization in the lower phosphatized portions of the crust. Iron (Fe) similarly demonstrates spatial complexity with respect to concentration and mineralogy, but lacks the dynamic range of oxidation state seen for Mn. Micrometer-scale measurements of metal abundances reveal complex element associations between trace elements and the two major oxide phases, which are not typically resolvable via bulk analytical methods. These findings provide evidence of post-depositional processes altering chemistry and mineralogy, and provide important geochemical context for the interpretation of element and isotopic records in ferromanganese crusts.

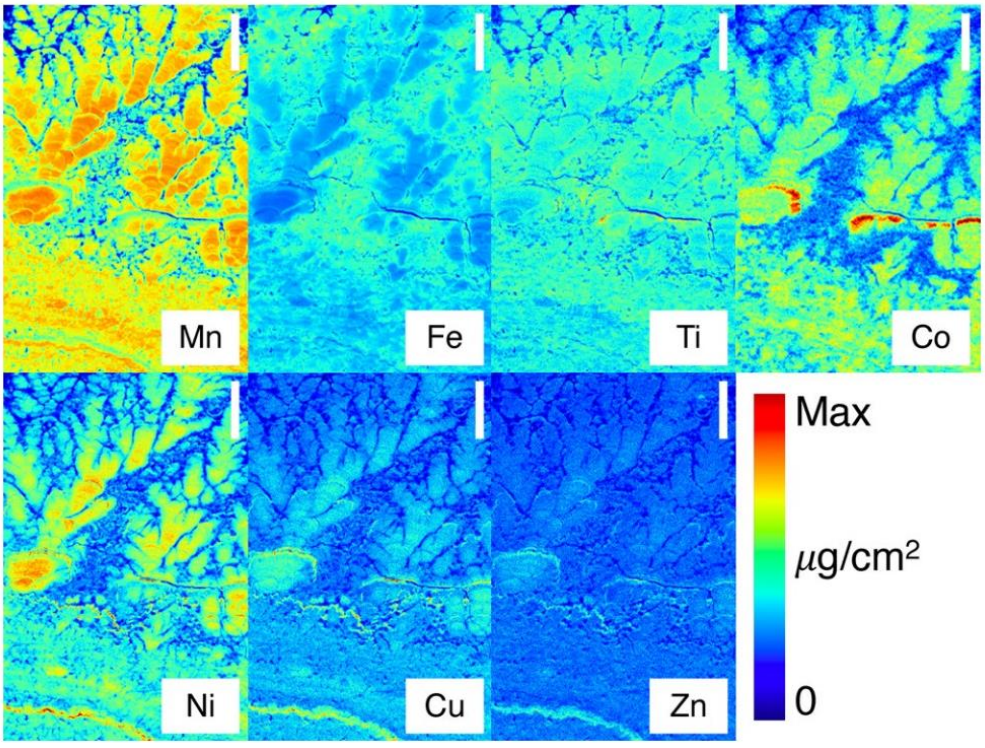

Figure 1. Micro X-ray fluorescence images of a representative section of ferromanganese growth structures (branching columns; laminations) in the upper section of the crust. Max concentrations are 1,350 μg/cm^2 (Mn and Fe), 100 μg/cm^2 (Ti), 50 μg/cm^2 (Co), 30 μg/cm^2 (Ni), and 10 μg/cm^2 (Cu and Zn). Scale bar (top right) represents 1 mm.

8. 甲烷、季风与千年尺度气候事件的调节

翻译人：杨会会 11849590@mail.sustech.edu.cn

Thirumalai K, Clemens S C, Partin J W et al. ***Methane, Monsoons, and Modulation of Millennial-Scale Climate****[J].Geophysical Research Letters, 2020, 47, e2020GL087613 https://doi.org/10.1029/2020GL087613*

摘要： 地球轨道的几何形状通过调节太阳辐射变化对气候产生深远的影响。更新世的记录揭示以突变和快速摆动为特征的千年尺度的气候变化，叠加在轨道驱动的气候变化上。然而，轨道驱动调节这些千年尺度变化的幅度和时间的程度还不清楚。这里我们将从两个具有良好定年结果，且都与岁差周期有关的记录中分离出千年尺度变化（MMV）的幅度。这两个记录分别是中国石笋 $\delta^{18}O$ 记录（通常解译为亚洲季风强度指标）和大气甲烷记录。在千年尺度上（1-10 kyr），我们发现岁差直接调节甲烷的 MMV，而不是石笋 $\delta^{18}O$ 的 MMV，这与南极冰芯 $\delta^{18}H$ 的 MMV 惊人地相似。一种解释是甲烷的 MMV 响应中高纬度日照的变化，而石笋是受内部气候反馈的调节。

ABSTRACT: Earth's orbital geometry exerts a profound influence on climate by regulating changes in incoming solar radiation. Superimposed on orbitally paced climate change, Pleistocene records reveal substantial millennial-scale variability characterized by abrupt changes and rapid swings. However, the extent to which orbital forcing modulates the amplitude and timing of these millennial variations is unclear. Here we isolate the magnitude of millennial-scale variability (MMV) in two well-dated records, both linked to precession cycles (19,000 - and 23,000-year periodicity): composite Chinese speleothem $\delta^{18}O$, commonly interpreted as a proxy for Asian monsoon intensity, and atmospheric methane. At the millennial timescale (1,000–10,000 years), we find a fundamental decoupling wherein precession directly modulates the MMV of methane but not that of speleothem $\delta^{18}O$, which is shown to be strikingly similar to the MMV of Antarctic ice core $\delta^{2}H$. One explanation is that the MMV of methane responds to changes in midlatitude to high-latitude insolation, whereas speleothem $\delta^{18}O$ is modulated by internal climate feedbacks.

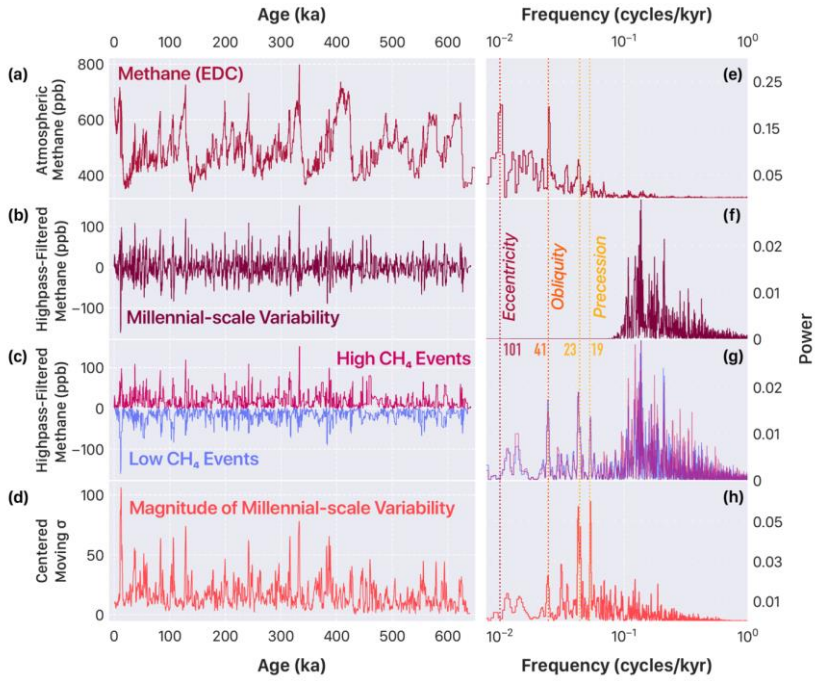

Figure 1. Orbital and millennial-scale atmospheric methane variability over the past 640 kyr. (a) EPICA Dome C record of CH_4, (b) its millennial-scale variability calculated as the 10-kyr high-pass filtered record of the original time series, (c) high-value and low-value CH_4 in the high-pass filtered record, and (d) the magnitude of millennial-scale variability (MMV) calculated as the centered rolling standard deviation of the high-pass filtered record using 2-kyr sliding windows (100-year step). (e–h) Periodograms of corresponding time series using the Lomb-Scargle methodology. Primary orbital frequencies are marked with dashed lines (19 and 23—precession; 41—obliquity; 101—eccentricity). Note different scaling for power spectral density. Strong peaks in the precessional band in the low-CH_4, high-CH_4, and MMV record indicate that insolation modulates the amplitude of millennial variations in atmospheric methane.

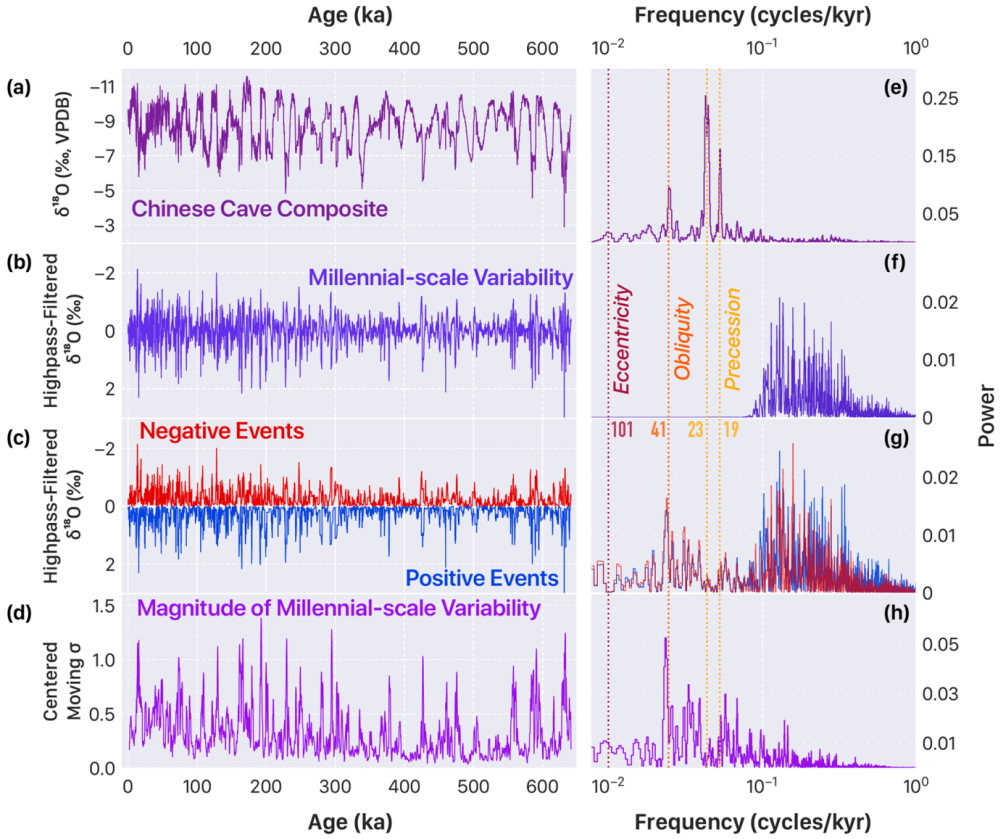

Figure 2. Orbital and millennial-scale variability in the composite Chinese speleothem record over the past 640 kyr. (a) Composite Chinese speleothem $\delta^{18}O$, (b) its millennial-scale variability calculated as the 10-kyr high-pass filtered record of the original time series, (c) negative-value and positive-value $\delta^{18}O$ in the high-pass filtered record, and (d) the magnitude of millennial-scale variability calculated as the centered rolling standard deviation of the high-pass filtered record using 2-kyr sliding windows (100-year step). (e–h) Periodograms of corresponding time series using the Lomb-Scargle methodology. Primary orbital frequencies are marked with dashed lines (19 and 23—precession; 41—obliquity; 101—eccentricity). Note different scaling for power spectral density. Despite that the "raw" $\delta^{18}O$ record contains strong concentrations of variance in the precessional band, the lack of peaks in the negative and positive events as well as in the MMV record suggest that precession does not modulate the envelope of millennial-scale $\delta^{18}O$ variations in the composite Chinese speleothem record.

9. 全新世以来，东亚冬季风的早期的减弱和中晚期增强

翻译人：王浩森 11930841@mail.sustech.edu.cn

Kang S J, Du J H, Wang N et al. ***Early Holocene weakening and mid- to late Holocene strengthening of the East Asian winter monsoon*** *[J]. Geology, 2020. 48: 1043-1047. https://doi.org/10.1130/G47621.1*

摘要：全新世以来，东亚冬季风（EAWM）的亚轨道尺度变化及其机制存在争议，部分原因是缺乏中国黄土的高精度记录。本文基于中国黄土高原的三个黄土剖面的光学激发发光测年法和粒度分析，重建了全新世以来 EAWM 强度的高分辨率信息。 EAWM 在全新世早期（约公元前 11.7-6.5 年）期间显示出持续的减弱趋势，而在全新世中晚期（约公元前 6.5 年以来）期间呈增强趋势。我们认为这分别是由北半球高纬度地区冰量和中高纬度地区北半球大气温度变化引起的。我们还观察到 EAWM 与东亚夏季风之间存在反相关关系。我们的发现为有关全新世 EAWM 变化的辩论提供了有力的解决方案，并有助于了解 EAWM 强度未来的潜在变化。

ABSTRACT: Sub-orbital-scale variations of the East Asian winter monsoon (EAWM) and its mechanisms during the Holocene are controversial, partly due to the lack of high-quality records from Chinese loess. Here, we present high-resolution reconstruction of Holocene EAWM intensity based on optically stimulated luminescence dating and grain-size analysis from three loess sections taken from the Chinese Loess Plateau. The EAWM showed a persistent weakening trend during the early Holocene (ca. 11.7–6.5 kyr B.P.) and a strengthening trend during the mid- to late Holocene (since ca. 6.5 kyr B.P.). We propose that this was caused by changes in high-latitude Northern Hemisphere ice volume and middle- to high-latitude Northern Hemisphere atmospheric temperatures, respectively. We also observed an anti-correlation between EAWM and East Asian summer monsoon. Our findings provide a robust solution to the debate regarding Holocene EAWM changes and contribute to the understanding of potential future variations in EAWM intensity.

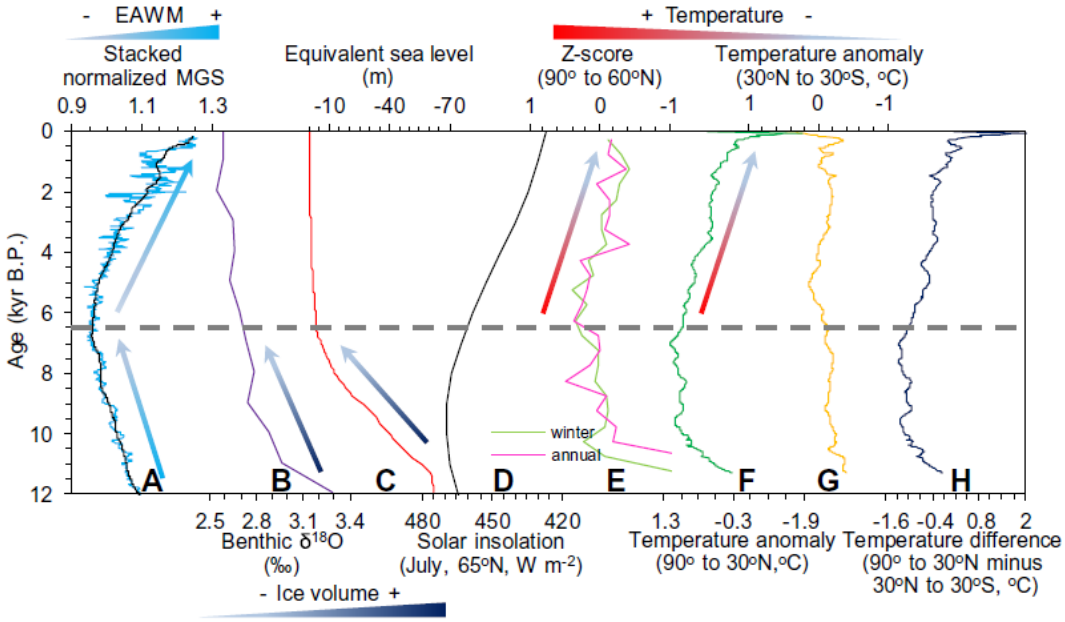

Figure 1. Comparisons between stacked normalized mean grain size (MGS) record and dynamic records. (A) Stacked normalized MGS (this study; see Fig. 2D). (B) Stacked benthic $\delta^{18}O$ (Lisiecki and Raymo, 2005). (C) Ice-volume-equivalent sea level relative to present (Lambeck et al., 2014). (D) Northern Hemisphere July insolation at 65° N (Berger and Loutre, 1991). (E) Standard score (z-score, global composite) of stacked temperature records (90° –60° N; Kaufman et al., 2020). (F) Middle- to high-latitude Northern Hemisphere (90° –30° N) temperature anomaly referenced to the A.D. 1961–1990 instrumental mean (Marcott et al., 2013). (G) Low-latitude (30° N to 30° S) temperature anomaly referenced to the A.D. 1961–1990 instrumental mean (Marcott et al., 2013). (H) Difference between middle- to high-latitude Northern Hemisphere (90° –30° N) and low-latitude (30° N to 30° S) temperature anomalies (Marcott et al., 2013). Blue-gradient arrows and wedge, and thick gray horizontal dashed linen are the same as those in Figure 2D. Dark-blue-gradient arrows and wedge indicate the changing trends of ice volume. Red-gradient arrows and wedge indicate the changing trends of temperature.

10. 维度辐射梯度控制的南北半球全新世降水异常同步性

翻译人：郑威　11930589@mail.sustech.edu.cn

Vidal-Cordasco M, Nuevo-López A. ***Resilience and vulnerability to climate change in the Greek Dark Ages*** *[J]. Journal of Anthropological Archaeology, 2020, 61: 101239. https://doi.org/10.1016/j.jaa.2020.101239*

摘要：青铜时代晚期的危机传统意义上被认为是地中海东部地区近代史的转折点。从公元前13世纪到公元前11世纪，爱琴海地区经历了年降雨量急剧减少、大量城市中心的毁坏或收缩、严重的人口紧缩、斗争增加、以及定居模式的变化。各种假说曾经被提出来解释这些转变，然而，鲜有研究明确审视了造成这场危机的各种因素之间的复杂且动态的关系。在本研究中，我们使用了一个基于代理的模型来探讨（a）干旱、（b）降雨量变化、（c）袭击的强度、（d）土壤侵蚀和（e）依赖于农业的饮食如何影响（a）人类对可耕种土地的压力、（b）人口行为、（c）定居模式、（d）商业网络和（e）迁徙。模拟得到的结果与考古记录有一致性，这表明了土壤退化、降雨变化和依赖于农业的饮食放大了青铜时代晚期和铁器时代早期气候变化带来的社会生态影响。

ABSTRACT: The Late Bronze Age crisis has traditionally been considered a turning point in the recent prehistory of the eastern Mediterranean. Between the 13th and 11th centuries B.C., the Aegean area experienced a dramatic reduction in the annual precipitation, the destruction or shrinkage of a large number of urban centres, critical demographic constrictions, an increase in struggles, and changes in settlement patterns. Various hypotheses have been proposed to explain these transformations; however, very few studies have explicitly examined the complex and dynamic set of relationships between the parameters that contributed to this crisis. In this study, we use an agent-based model to explore how (a) aridity, (b) rainfall variability, (c) intensity of raiding, (d) soil erosion and (e) dietary reliance on agriculture could have influenced (a) the human pressure for cultivable lands, (b) demographic behaviour, (c) settlement patterns, (d) commercial networks and (e) migrations. Outputs obtained from the simulations are consistent with the archaeological

record and suggest that soil degradation, rainfall variability and dietary reliance on agriculture could have amplified the socio-ecological effects of the climatic change in the Late Bronze Age and the Early Iron Age.

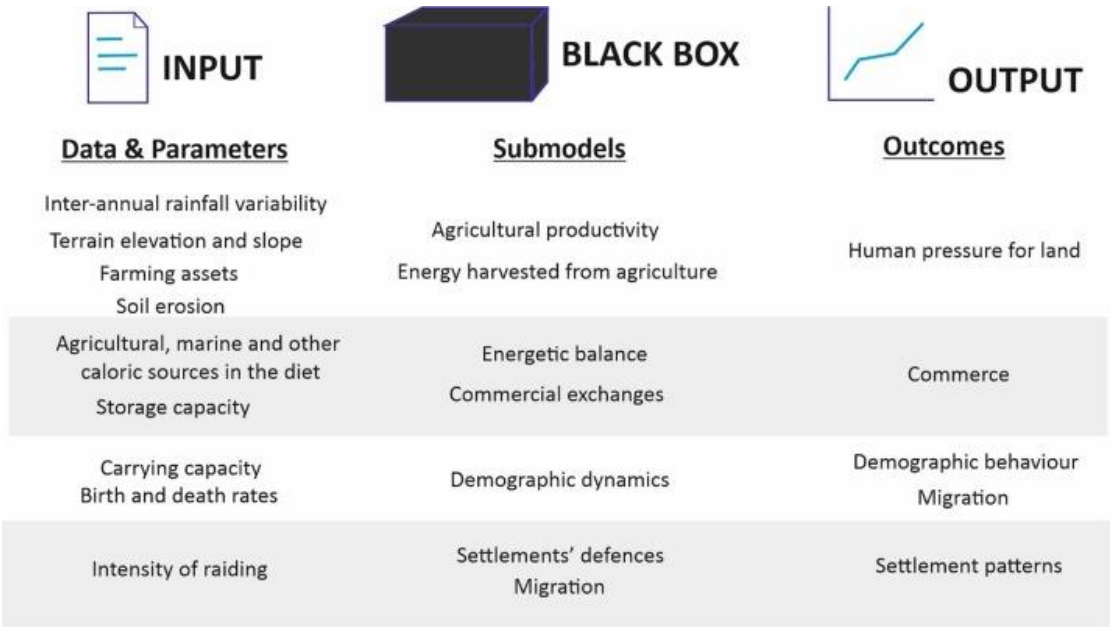

Figure 1. Graphic summary of the main parameters, submodels and outputs of the Bronze Age Collapse (BACO) model.

11. 全新世早期东海西部潮滩演化对海平面上升事件的响应

翻译人：李海 12031330@mail.sustech.edu.cn

Yan D, Wünnemann B, Gao S, Zhang Y, ***Early Holocene tidal flat evolution in a western embayment of East China Sea, in response to sea level rise episodes*** *[J]. Quaternary Science Reviews, 2020. 250, 106642.*

https://doi.org/10.1016/j.quascirev.2020.106642

摘要：末次冰盛期以来，东海沿海地区介于长江口和杭州湾之间的潮滩与沉积物的运输/扩散和海平面的变化相互联系，这是数十年来一直进行的严格研究。在这里，我们重点关注响应全新世早期海平面上升而在前海洋影响力最西端的潮滩的演变。我们将沉积物成分，介形虫，矿物质，有机质和碳酸盐含量与两个钻孔沉积物的端元分析和主成分分析相结合，并在靠近杭州以北的前海洋影响区西部边界的一个考古现场进行了分析。这些地点的潮滩对全新世早期的形态变化和海平面变化非常敏感。我们的数据显示出潮滩形成的两个主要阶段：i）早期形成阶段（9.5-8.0 cal ka BP），沉积物供应量低，平均相对海平面上升（MRSL）的相关速度减慢，ii）随着沉积物供应增加，暴风雨发生以及在强大的 MRSL 上升接近其当前水平的情况下，使得快速沉积过程（8.0-7.5 cal ka BP）而进入了扩张期。最后阶段（7.6–7.5 cal ka BP）记录了 MRSL 的静止状态/下降状态。这些推论与先前发布的局部到区域海平面曲线相匹配，但与全局和建模区域曲线不同。我们提出了与全新世早期不稳定的气候条件有关的，暴风雨事件加剧和夏季季风降雨变化更大的影响，这影响了河流泄流量和相关的沉积物在 9.5 至 7.6 cal BP 之间向东海内陆的迁移。潮汐淹没的沿海小海湾中海湾区域的沉积序列对海平面上升事件和相关的气候变化敏感。

Abstract The tidal flat in the coastal region of the East China Sea between the Yangtze estuary and Hangzhou Bay in China, interlinked with sediment transport/dispersal and sea level changes since the Last Glacial Maximum, has been a matter of rigorous research for decades. Here we focused on the evolution of the tidal flat at the westernmost extend of former marine influence in response to early Holocene sea level rise. We used sediment composition, ostracods, minerals, organic matter and carbonate contents in combination with endmember modelling analyses and principal component analysis from two sediment cores and an archaeological site close to the western boundary of former marine influence north of the Hangzhou city. The tidal flats at these sites were

very sensitive to morphological changes and to sea level variation during the early Holocene. Our data show two major phases of tidal flat formation: i) an early formation stage (9.5–8.0 cal ka BP) with low sediment supply and related slow-down of the mean relative sea level rise (MRSL), followed by ii) the expansion phase with increased sediment supply, storm occurrence as well as fast depositional processes (8.0–7.5 cal ka BP) under a strong MRSL rise close to its present level. A stillstand/decline of MRSL was recorded for the last episodes (7.6–7.5 cal ka BP). The inferences match previously published local to regional sea level curves but differ from the global and modelled regional ones. We propose a connection with early Holocene unstable climatic conditions with intensified storm events and stronger variations in summer monsoon rainfall that affected river discharge and related sediment transport to the inner shelf of the East China Sea between 9.5 and 7.6 cal ka BP. Sedimentary sequences of bayhead areas in tidally-drowned coastal embayments are sensitive to sea level rise episodes and the relevant climate changes.

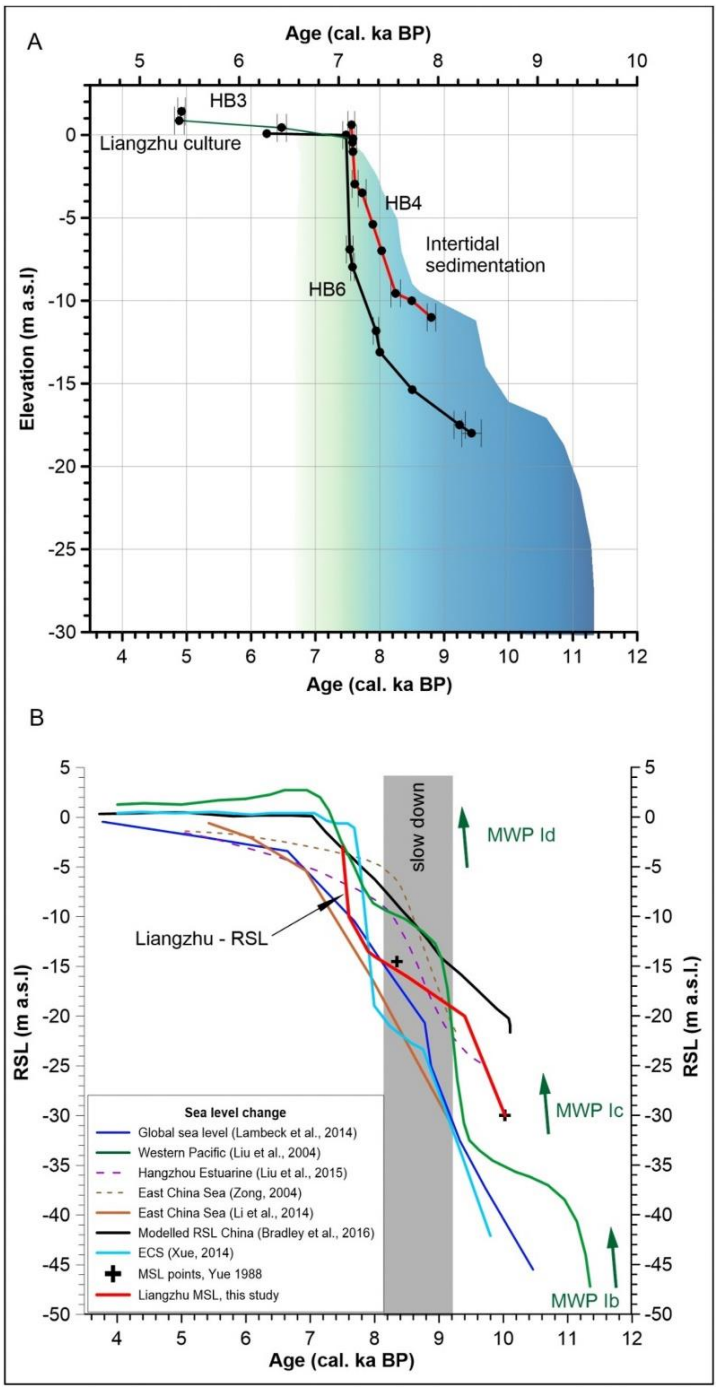

Figure 1. Sedimentation of tidal flats at cores sites HB4 and HB6 (A) and reconstructed mean relative sea level change (B) in comparison with published sea level records for the early and middle Holocene.

12. 印支地块中生代南向运动和顺时针旋转：来自古地磁和碎屑锆石 U-Pb 年代学约束

翻译人：周洋 zhouy3@sustech.edu.cn

Yan Y G, Huang B C, Zhao J et al. ***Large southward motion and clockwise rotation of Indochina throughout the Mesozoic: Paleomagnetic and detrital zircon U–Pb geochronological constraints*** *[J]. Earth and Planetary Science Letters, 2017, 459, 264–278.*

摘要：为了了解印支地块的构造演化过程，对泰国东北部中生代地层 Huai Hin Lat 和 Nam Phong 组的古地磁学和碎屑锆石 U-Pb 年代学进行了研究。碎屑锆石 U-Pb 年代学结果显示这两套地层的最大沉积年龄（MDA）分别为 227 Ma 和 215 Ma，这也表明了 Khorat Plateau 盆地在中-晚侏罗世沉积物源发生了转变。古地磁结果显示，不同岩性、层面产状、磁性载体和极性的样品之前的 D_g / I_g = 21.4°/ 38.1°（k_g = 19.5，α_{95}= 9.6°），倾斜校正后为 Ds / Is = 43.0°/ 48.0°（k_s = 47.4，α_{95}= 6.1°，N = 13）。经修订的印支地块中生代 APWP 古纬度（参考点为 22ºN，102ºE）在晚三叠世 Norian 期间为 33.4±7.2ºN，在晚三叠-早侏罗世为 25.9±5.9ºN，晚侏罗-早白垩世为 23.9±8°N，早白垩世为 27.5±3.2°N，晚白垩世为 24.5±4.9°N， 相应的偏角分别为 45.2±8.6°，38.0±6.6°，36.3±8.8°，29.6±3.6°和 24.9±5.4°。这些数据表明在中生代期间印支地块明显南移并伴随着顺时针旋转。华南和华北拼合过程中对印支地块的重建表明，在晚三叠世的 Norian 期，印支地块的纬度要高于华南地块，在早侏罗-早白垩世期间，没有明显的相对极移发生。我们的研究支持白垩纪之后的构造挤压模型，印支地块相对于华南地块向东南挤出，自晚白垩世以来位移量估计为 1000±850 km。

ABSTRACT: We report a combined paleomagnetic and U–Pb geochronologic study of sedimentary rocks from the Huai Hin Lat and Nam Phong formations of Mesozoic age in NE Thailand in order to provide independent constraints on the tectonic movement of the Indochina Block during convergence of the major blocks now comprising East Asia. The maximum allowable depositional age of the two formations is estimated to be 227 Ma and 215 Ma, respectively, from detrital zircon U–Pb geochronologic analysis which also indicates a sediment source transition in the Khorat

Plateau Basin during the Middle–Late Jurassic. A formation mean paleomagnetic direction of D g/I g = 21.4◦/38.1◦ (kg = 19.5, α95 = 9.6◦) before and Ds/Is = 43.0◦/48.0◦ (ks = 47.4, α95 = 6.1◦, N = 13) after tilt correction is derived from samples with different lithologies, bedding attitudes, magnetic carriers and polarities and yields a positive fold test. Hence, the magnetization is likely primary. The revised Mesozoic APWP of the Indochina Block yields paleolatitudes (for a reference site of 22◦N, 102◦E) of 33.4 ± 7.2◦N during the Norian Late Triassic, 25.9± 5.9◦N during the Late Triassic to Early Jurassic, 23.9 ± 8◦N during the Late Jurassic to Early Cretaceous, 27.5 ± 3.2◦N during the Early Cretaceous and 24.5 ± 4.9◦N by the Late Cretaceous; corresponding declinations are 45.2 ± 8.6◦, 38.0 ± 6.6◦, 36.3 ± 8.8◦, 29.6 ± 3.6◦ and 24.9 ± 5.4◦ respectively. These data indicate a significantly southward displacement accompanied by clockwise rotation during the Mesozoic. A reconstruction of the Indochina Block within the now well-studied merging process of South China and North China indicates that the Indochina Block was located at a higher latitude than the South China Block during the Norian stage of Late Triassic times whilst no significant relative poleward displacement apparently occurred during the Early Jurassic to Early Cretaceous interval. Our study supports a post-Cretaceous tectonic extrusion model with a southeastward displacement of Indochina with respect to the South China Block estimated to be 1000 ± 850 km since the Late Cretaceous.

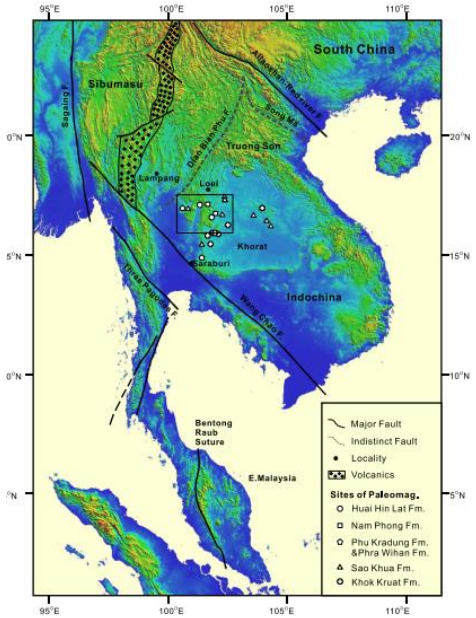

Figure 1. A digital elevation model with schematic tectonic units of Southeast Asia and surrounding regions (modified from Takemoto et al., 2009; Metcalfe, 2013; Burrett et al., 2014). Abbreviations: Fm.: Formation, F.: Fault, E. Malaysia: Eastern Malaysia.